

Arbeit zur Erlangung des akademischen Grades
Bachelor of Science

**Neural network based
signal-background classification for the
differential single top+photon
measurement at the ATLAS experiment**

Cihad Gözsüz
geboren in Dortmund

2021

Lehrstuhl für Experimentelle Physik IV
Fakultät Physik
Technische Universität Dortmund

Erstgutachter: Prof. Dr. Johannes Erdmann
Zweitgutachter: Prof. Dr. Johannes Albrecht
Abgabedatum: 13. July 2021

Abstract

The investigation of the top quark coupling to the photon offers a critical test of the Standard Model. Differential measurement of the $tq\gamma$ process of the Standard Model would grant new insights into this electromagnetic coupling of the top quark. Regarding a measurement of $tq\gamma$ with the full Run-2 dataset at the ATLAS experiment, a neural network is trained on data from Monte Carlo simulations to discriminate background processes from the $tq\gamma$ signal process. Certain features of events are provided as input to the neural network. In this thesis, the influence of these input features on the neural network's ability to separate signals from the background is investigated, by first calculating correlations of the features with the NN output and then examining how different requirements on the features influence the composition of the output. This provides knowledge into which event features are essential characteristics to understand the electromagnetic coupling of the top quark.

Contents

1	Introduction	1
2	Single top quark production with a photon in the Standard Model	2
2.1	A brief overview of the Standard Model	2
2.2	The $tq\gamma$ process in the Standard Model	4
3	Measurement of $tq\gamma$	6
3.1	The ATLAS Experiment	6
3.2	Object Reconstruction at the ATLAS experiment	7
3.3	Background contributions from similar processes	9
4	Monte Carlo samples and event selection	11
4.1	Generation of Monte Carlo samples	11
4.2	Event selection	12
5	The Neural Network used for signal-background classification	13
5.1	Short introduction to neural networks	13
5.2	The neural network architecture	13
5.3	Input features for the neural network	14
5.4	Performance and distribution of the NN output	17
6	Differential analysis of the NN output	19
6.1	Weighted correlations of input features with the NN output	19
6.2	NN output distribution dependence on photon p_T^γ and fjet+photon energy $E_{fj+\gamma}$	22
7	Conclusion	25
8	Appendix	26
9	Danksagung	34
	Bibliography	35

1 Introduction

The Standard Model (SM) of particle physics describes the nature of discovered elementary particles and three of the four fundamental interactions: the strong, weak and electromagnetic interaction. Only the gravitational interaction is not covered by the theory. The SM has been researched extensively and is widely regarded as the most successful theory. However, the SM contains several conceptional problems and is unable to explain all phenomena. For instance, the existence of dark matter is not accounted for in the SM. The many problems of the SM motivate the search for physics beyond the Standard Model (BSM). It is therefore essential to test and research the limits of this theory.

Many tests of the Standard Model involve the top quark, the most massive elementary particle. One such test would be the search for the single production of a top quark in association with a photon in proton-proton collisions ($pp \rightarrow tq\gamma$). The process is sensitive to the electroweak coupling of the top quark. As this coupling is a critical parameter of the SM, a precise measurement of the cross-section for this process may give new insights into this parameter. The $tq\gamma$ process has not yet been observed but the CMS Collaboration reported evidence for it in 2018 corresponding to 4.4 standard deviations [23]. Since the discovery of the process should be possible with the full Run-2 dataset, studies with regard to a differential measurement are carried out in this thesis. The differential measurement would yield a close examination of the structure of the electromagnetic coupling of the top quark.

As $tq\gamma$ is a rare process of the SM, a significant amount of background occupies the measurement region and the signal to background ratio is inherently small. A classifying neural network (NN) is implemented to discriminate the signal process $tq\gamma$ from the background processes. This NN is trained on simulated data and receives characteristic event variables of $tq\gamma$ as input. Studying the significance and effects of different input parameters on the output may help narrow down or provide conditions for the event selection to optimise background suppression which would be useful for the differential analysis. Additionally, the investigation of these input features could provide vital insights into the nature of the $tq\gamma$ process. In this thesis, the correlations of characteristic features of $tq\gamma$ with the NN output are analysed. Subsequently, two input features, the transverse momentum of the photon p_T^γ and the sum of the forward jet energies and the photon energy, are further studied. Changes in the NN output distribution are examined for different requirements on the kinematic variables.

2 Single top quark production with a photon in the Standard Model

2.1 A brief overview of the Standard Model

The Standard Model (SM) of particle physics, a quantum field theory, describes today's best theory of particle physics. In the SM, there are different kinds of elementary particles and three fundamental forces of nature: the electromagnetic force, the strong force and the weak force. Every force coincides with an elementary particle, called a boson, that acts as a mediator of the interaction. Another group of particles are called the fermions, and they only interact with these bosons if they have specific quantities, which are represented by their quantum numbers.

The fermions have spin $s = \frac{1}{2}$ and can be divided into two separate groups. The first group, named quarks, are colour charge carrying fermions. There are three up-type quarks (up, strange and top) with an electric charge of $q = +\frac{2}{3}e$ and three down-type quarks (down, charm and bottom) with an electric charge of $q = -\frac{1}{3}e$. The second group are the leptons. Three leptons (electron, muon and tau) have an electric charge of $q = +1e$. Furthermore, each of these leptons has a corresponding uncharged lepton partner called a neutrino. Three different families further categorize leptons and quarks. These quark and lepton families are ordered by mass and consist of an up-type quark, the corresponding down-type quark, a lepton and the corresponding neutrino. There is an anti-matter particle equivalent for all fermions where every charge-like quantum number has the opposite sign.

Particles with integer spin are called bosons. The first group of bosons, gauge bosons with spin $s = 1$, mediate the three fundamental forces. The gauge bosons with spin $s = 1$ are: *gluons* g , *photons* γ , Z and W^\pm . The Higgs boson H is the only boson with spin $s = 0$.

Gluons are colour charged and mediate the strong force between colour charged particles, including themselves. The six colour charges are *red, green, blue* and their anticolour counterpart. The strong force draws particles with colour together until a colour neutral state is achieved. This can occur when one quark bonds with a quark of the opposite colour, forming a meson. It can also occur when three quarks with *red, green, blue* colour charges respectively together form the colour neutral

2.1 A brief overview of the Standard Model

Baryon. The strong force becomes stronger the further quarks are repelled from the colour neutral state. If quarks get repelled for a sufficiently high distance, two new quarks are formed, which then bond with the repelled. This process is called colour confinement and can occur many times in a row for higher energies, forming a shower of mesons and baryons. Photons mediate the electromagnetic (EM) between electrically charged particles. The massive bosons, Z and W^- as well as W^+ mediate the weak force. The weak force only acts on left-handed particles (and right-handed antiparticles). Here, left-handedness means that the spin direction is opposite to the direction of the momentum of the particle. Right-handed particles have their spin and momentum pointing at the same direction. The W^\pm bosons are electrically charged, $q = \pm 1e$, and change the flavour of a quark when coupling to it. The flavour refers to the species of a fermion.

The Higgs boson arises from the electroweak theory. The Higgs mechanism provides an explanation for the presence of massive leptons and bosons by breaking the electroweak symmetry. The fermions acquire their mass by coupling with the Higgs boson via the so-called Yukawa interaction. Before the breaking of the electroweak symmetry, the gauge bosons exist as the electroweak eigenstates W^1 , W^2 , W^3 and B . The breaking of this symmetry mixes W^3 and B into the mass eigenstates Z and γ . The eigenstates W^1 and W^2 mix into the massive eigenstates W^+ and W^- .

An overview of the elementary particles in the Standard Model is given in figure 2.1.

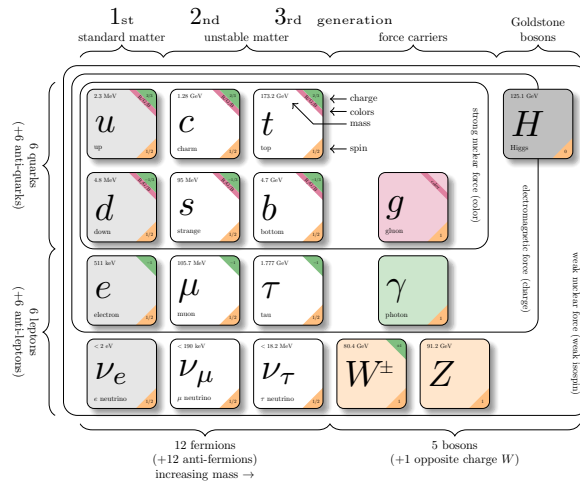


Figure 2.1: Elementary particles of the Standard Model alongside their properties [9].

2.2 The $tq\gamma$ process in the Standard Model

The top quark is an up-type quark and the most massive quark of the Standard Model with a mass of $m_t = 173.76 \pm 0.3 \text{ GeV} (S = 1.2)$ [25]. Additionally, the top quark has a very small decay width of $\Gamma = 1.42^{+0.19}_{-0.15} \text{ GeV} (S = 1.4)$ [25] because of its high mass. This is one reason why the top quarks unlikely to build any bound states and always decay shortly after production. Only their decay products are observable and can be retraced back to the top quark.

Top quarks can be produced in three different channels: In the t -channel (tq), where a single top quark is produced when a bottom quark exchanges a W -boson with another quark, the s -channel (tb), where the top quarks are produced in top-antitop-pairs, and the tW -channel, where a gluon and a bottom couple and then decay into a single top and a W boson. In this thesis, the focus lies primarily on the t -channel production of the top quark. The top quark was first discovered in pair production at the Tevatron in 1995 during a proton-antiproton collision experiment (CITE). In 2009, the D0 [5] and CDF [4] collaborations also separately confirmed the observation of the t -channel top quark production at the Tevatron. The combined results are available in reference [16]. The CMS experiment at the Large Hadron Collider (LHC) of CERN [11] reported evidence for the t -channel single production of top quarks in association with a photon ($tq\gamma$) with a significance corresponding to $\sigma = 4.4$. The fiducial cross section was measured to be $\sigma(pp \rightarrow tq\gamma)(t \rightarrow \mu\nu b) = 115 \pm 17(stat) \pm 30(syst) \text{ fb}$ for the photon transverse momentum $p_T^\gamma > 25 \text{ GeV}$ [24].

For this thesis, the $tq\gamma$ -events are produced in proton-proton-collisions inside the ATLAS experiment. The ATLAS is discussed in detail in chapter 3. The production of processes in this experiment occurs with elementary particles inside of the protons, called partons. For the production of the $tq\gamma$ -process, one gluon provided by the protons may produce a bottom-antibottom-quark pair. The bottom quark may then exchange a W -boson with a quark, turning the bottom quark into a top quark and changing the flavour of the quark. This top quark may then radiate a photon. It is essential to mention that while this thesis focuses on the top-photon vertex, the photon can be radiated from any charged particle elsewhere in the process. For instance, the bottom quark after the decay of the top may produce a photon. Afterwards, the top quark decays into a W^+ -boson and a bottom quark. The W^+ -boson then decays either into an antilepton and neutrino pair or a quark-antiquark pair of opposite quark types. However, only the leptonic decay mode is considered in this thesis.

In Figure 2.2 the leading order Feynman diagram for the $tq\gamma$ production is depicted. The charge conjugated diagram is not shown, but also considered in this thesis.

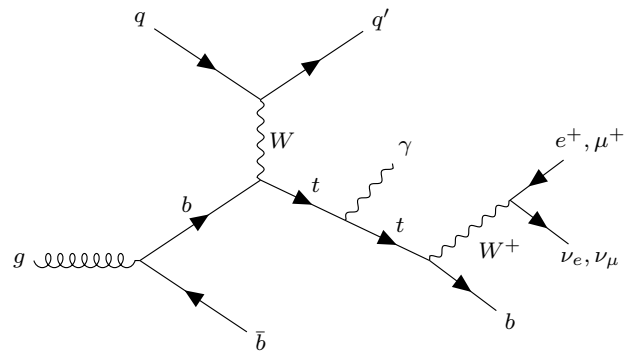


Figure 2.2: Leading order Feynman diagram of the $tq\gamma$ process in the Standard Model.

3 Measurement of $tq\gamma$

3.1 The ATLAS Experiment

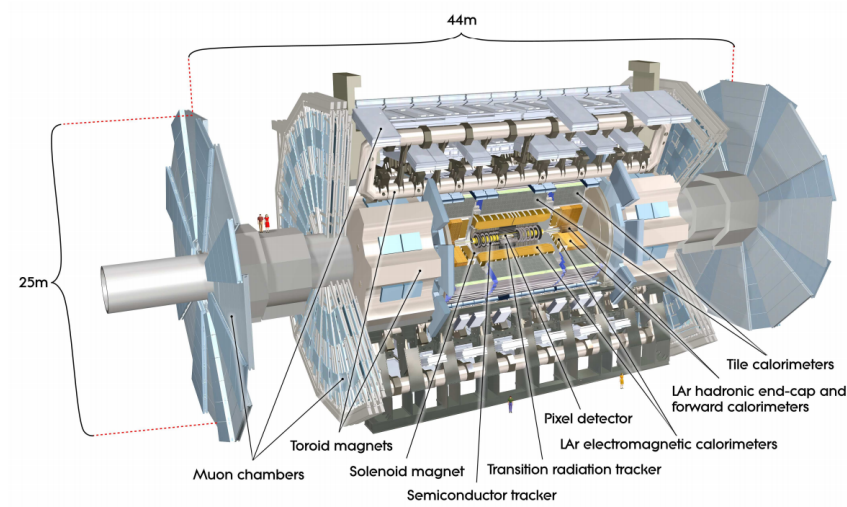


Figure 3.1: Schematic visualisation of the ATLAS Detector [15].

The European Organization for Nuclear Research, known as CERN, located in Geneva, has various experiments studying elementary particles through the collision of mainly heavy ions and protons. The Large Hadron Collider (LHC), the largest particle accelerator of CERN [8], has a circumference of 27km and can collide particles with a center of mass energy of up to $\sqrt{s} = 13 \text{ TeV}$.

The LHC consists of four main experiments: the ALICE, the LHCb, the CMS and the ATLAS experiments [15]. The research in this thesis is done with the help of the largest of these experiments, the ATLAS experiment. Figure 1 visualizes the structure of the ATLAS detector. A coordinate system needs to be defined in order to discuss the construction of the experiment and positions of objects. Three different coordinates are used to describe positions inside the detector: First, the azimuthal angle ϕ , which ranges from 0 to 2π . Next, the pseudorapidity η , which is defined to be $\eta = -\ln(\tan \theta)$, where θ is the angle to the beam axis. The smaller θ

is, the higher the pseudorapidity. And lastly, a distance ΔR , which can be defined in the ϕ - θ -plane as $\Delta R = \sqrt{(\Delta\phi)^2 + (\Delta\eta)^2}$.

The ATLAS detector is built symmetrically around the particle beam and can be divided into three subdetectors:

The inner detector [7] tracks charged particles just after the collision. It consists of three different systems of sensors in a magnetic field parallel to the beam. These sensors are the pixel detector, the semiconductor tracker and a transition radiation tracker to track particles with gas-filled tubes.

In the EM calorimeter, metal layers (tungsten, copper or lead) absorb incoming particles and convert them into lower-energy particles called a shower [21]. The calorimeters detect showers produced by electrons (and positrons), photons and hadrons. The barrel part of this calorimeter covers the pseudorapidity range $|\eta| \leq 1.475$ and the end-cap components cover $1.375 < |\eta| < 3.2$. Hadrons do not deposit all of their energy into the EM calorimeter; their showers get absorbed by steel layers in the hadronic calorimeter [3] behind the EM calorimeter. Here, plastic scintillating tiles produce photons that get converted into an electric current. The scintillating tiles cover the region $|\eta| < 1.7$. The region $1.5 < |\eta| < 4.9$ is then used by the copper + liquid argon and tungsten + liquid argon calorimeter.

The muon spectrometer measures trajectories of muons with the help of a magnetic field. Muons are the only detectable particles that pass through all inner detector elements without losing a lot of energy. The spectrometer detects muons in the range of $|\eta| < 2.7$. Monitored drift tubes measure pseudorapidities up to $|\eta| = 2.0$ and cathode strip chambers cover higher pseudorapidities.

3.2 Object Reconstruction at the ATLAS experiment

3.2.1 Reconstruction of photons

Photons mostly do not leave tracks inside the inner detector. They are reconstructed from clusters in the electromagnetic calorimeter [21]. Photon candidates need to pass the *Tight* identification [1] criteria with the transverse momentum being $p_T > 20 \text{ GeV}$ and $|\eta| < 2.3$. Photon candidates in the calorimeter transition region $1.37 < |\eta| < 1.52$ are excluded.

3.2.2 Reconstruction of electrons and muons

Leptons like an electron also produce clusters inside the electromagnetic calorimeter and leave charged particle tracks in the inner detector. All leptons in the calorimeter region $1.37 < |\eta| < 1.52$ are excluded. Electron candidates have to pass the tight likelihood identification (TightLH [1]) conditions of $p_T > 27 \text{ GeV}$ and $|\eta| < 2.47$. To reconstruct muons, charged particle tracks in the inner detector are matched with muon spectrometer tracks. Muon candidates are required to pass the Medium identification [2] with $p_T > 27 \text{ GeV}$ and $|\eta| < 2.5$.

3.2.3 Jets

Jets are showers of mostly mesons and fewer baryons in the hadronic calorimeter that result from the production of high energy quarks (colour confinement). They deposit some of their energy in calorimeter cells which then are combined into clusters by the anti- k_t algorithm [10] with a radius parameter of $R = 0.4$. It is then required that the cluster has a transverse momentum of $p_T > 25 \text{ GeV}$ and $|\eta| < 4.5$. If these conditions are met, the cluster is identified to be a jet.

Detector noise can lead to the misidentification of a jet. The nature of these misidentified jets has been studied thoroughly and a so-called "jet cleaning procedure" is used to tag them. Any event containing at least one "bad" jet is removed by the algorithm [14].

3.2.4 b-tagging

For the measurement of $tq\gamma$, the identification of jets produced by bottom quarks (b -tagging) must be made with high accuracy to distinguish *bottom* jets from *charm* jets. Here, the *DL1r* algorithm is implemented for b -tagging. Only jets passing 70% working point and $p_T > 20 \text{ GeV}$ are viewed as b -jets in this analysis. Detailed information on the *DL1r*-algorithm can be found in the references [17] and [18].

3.2.5 Missing transverse momentum E_T^{miss}

If all particles originating from the hard-scattering process are measured, there should be no magnitude for the sum of the transverse momentum p_T of all particles. Any measured magnitude is therefore attributed to an unmeasured particle. The missing transverse energy E_T^{miss} is consequently defined as the negative of this sum

and assigned to a neutrino, as neutrinos pass through detectors without losing practically any energy and therefore are undetectable in this experiment.

3.2.6 Short note on the reconstruction of the top quark

The missing transverse momentum E_T^{miss} is used to reconstruct the neutrino in the $tq\gamma$ process. Here, the z component of the neutrino's momentum is derived by requiring the invariant mass of the neutrino and the leading lepton to be equal to the W boson mass. The top quark is then reconstructed by combining the resulting four-momentum of the neutrino and the four-momenta of the lepton candidate and the b -jet [13].

3.3 Background contributions from similar processes

Various processes besides $tq\gamma$ are also accepted by the criteria for event selection 4.2. Contributions from these processes are considered background. Some background processes consist of "real" photons while a photon in other background processes are misreconstructed. The process $t\bar{t}\gamma$, the pair production of the top quark with a photon, holds the most similar final state. This process does have an additional b -jet because of the second top quark, but it may not get b -tagged correctly. If the decay of the other top quark also does not get correctly reconstructed, then the $t\bar{t}\gamma$ process virtually looks identical to $tq\gamma$. Next highest background contributions come from the production of a W -boson with a photon and jets, a Z -boson with a photon jets and $t\bar{t}$, which has a "faked" photon.

Table 3.1 lists these and more of these processes contributing to the background.

	Process	Explanation
1	$tq\gamma$	Single top+photon production
2	$t\bar{t}\gamma$	Top pair production with photon
3	$W\gamma + jets$	Production of W boson with a photon and jets
4	$Z\gamma + jets$	Production of Z boson with a photon and jets
5	$t\bar{t}$	Top pair production
6	$s\text{-}chan$	s -channel single top production (see Section 2.2)
7	tW	tW -channel single top production (see Section 2.2)
8	$t\text{-}chan$	t -channel single top production (see Section 2.2)
9	VV	Diboson production
10	$W + jets$	Production of W boson alongside jets
11	$Z + jets$	Production of Z boson alongside jets

Table 3.1: List of SM processes that contribute to background in the measurement of $tq\gamma$.

4 Monte Carlo samples and event selection

4.1 Generation of Monte Carlo samples

The simulation of a process is done in three steps: First, the event is generated by calculating corresponding matrix elements. Then the resulting electromagnetic and hadronic showers need to be modelled. Lastly, the detector itself needs to be simulated in order to account for the detector response and the reconstruction of events.

The framework `MADGRAPH5_AMC@NLO` is used for Monte Carlo (MC) simulations of the considered $tq\gamma$ process. `MADGRAPH5` is a matrix element generator that allows the interfacing of different packages for further simulation. The simulated events are generated at next-to-leading order (NLO) at the t -channel of single top production. The generator is interfaced to the package `PYTHIA v8.240`, which provides parton showers. The `MADSPIN` and `EVTGEN v1.6.0` packages give decay simulations of the top and bottom quark, respectively. Here, only leptonic decays of the top quark are considered.

Moving on to background processes, the $t\bar{t}$ process is modelled at leading order (LO) also using `MADGRAPH5_AMC@NLO v2.3.3` interfaced to `PYTHIA v8.212`. Simulation of $W\gamma$ +jets and $Z\gamma$ +jets events are produced at NLO using the `SHEPRA v2.2.2` and `SHEPRA v2.2.4` packages. For the $t\bar{t}$ process and t -, s -, tW -channels `POWHEG-BOX` is used where `PYTHIA v8.230` is again used as the showering program. The modeling here is performed in NLO in QCD.

The final events generated by `PYTHIA` are processed through an ATLAS detector simulation build with the `GEANT4` detector simulation toolkit [6]. This model of the ATLAS is reconstructs leptons, photons and jets from the detector response. To achieve this, the structure of the ATLAS detector as described in Section 3.1 is implemented the `GEANT4` based simulation. This includes a simulation of the inner detector, the electromagnetic calorimeter, the hadronic calorimeter and the muon spectrometer. Events are then reconstructed by analysing particles passing through each detector component as described in section 3.2.

The table 4.1 gives a summary of the generated samples and their generators.

Process	Generator
$tq\gamma$	<i>MadGraph5_aMC@NLO + Pythia8</i>
$t\bar{t}\gamma$	<i>MadGraph5 + Pythia8</i>
$W\gamma + jets$	<i>Sherpa 2.2.2</i>
$Z\gamma + jets$	<i>Sherpa 2.2.4</i>
$t\bar{t}$	<i>Powheg + Pythia8</i>
single top	<i>Powheg + Pythia8</i>
$W + jets$	<i>Sherpa 2.2.1</i>
$Z + jets$	<i>Sherpa 2.2.1</i>
Diboson	<i>Sherpa 2.2.2</i>

Table 4.1: List of generated samples alongside their generators.

4.2 Event selection

The selection criteria for events must hold the necessary conditions for a $tq\gamma$ -process. It also needs to have enough restrictions to reduce background contributions as much as possible. Signal events have precisely one lepton, at least one photon and one b -tagged jet in the final state. The lepton should have a transverse momentum higher than 20 GeV, the photons momentum higher than 27 GeV and the b -tagged jet has to pass the *DL1r*-algorithm with a 70% working point.

Additionally, the missing transverse energy E_T^{miss} ought to be above 30 GeV to account for the neutrino in the decay mode. Finally, to reduce leading background contributions from the $Z \rightarrow ee(\rightarrow \gamma)$ process, the invariant mass of the leading photon and an electron candidate $m_{e\gamma}$ is set to be in the range $80 \text{ GeV} < m_{e\gamma} < 110 \text{ GeV}$. Altogether, this makes up the following requirements for selected events:

1. At least one photon γ with $p_T > 20 \text{ GeV}$
2. Exactly one lepton with $p_T > 27 \text{ GeV}$
3. $E_T^{miss} > 30 \text{ GeV}$
4. Exactly one b -tagged jet passing 70% working point (WP) of the *DL1r*-algorithm.
5. Invariant mass of leading photon and electron candidate between values $80 \text{ GeV} < m_{e\gamma} < 110 \text{ GeV}$

5 The Neural Network used for signal-background classification

5.1 Short introduction to neural networks

Neural networks are loosely based on the human brain and are a means of doing machine learning, in which a computer learns to perform a task by analyzing data provided for training. In this thesis specifically, a fully connected neural network is used for classification purposes. The NN discriminates between the $tq\gamma$ signal events and background events by training on MC sample simulations (Section 4.1). Characteristic variables of the processes, which are discussed in detail in Section 5.3, are used as the input.

The NN is organized into layers of processing nodes. These processing nodes are densely interconnected between layers, and every connection weighted. During the *forward propagation*, where the NN is evaluated on labeled MC samples, computations in the NN propagate from the input layer to the output layer. An individual node in the inner layers receives values from nodes from the previous layer and sends a weighted sum of these values to nodes in the layer above. Nodes multiply received node values by weight value of the connection and add them together to a single value. Additionally, one number called the "bias" is added to the sum. The bias is a parameter specific to every node. During *backpropagation*, when the NN is being trained, weights and biases are continually adjusted until training data of the same sample yield similar results.

5.2 The neural network architecture

The NN is built implementing the Keras [12] library running on TensorFlow as backend[22]. Two different neural networks are trained to separate the signal from the background. One is trained on the zero-forward jet signal region ($0-fj$), and the other is trained on the At least one forward jet region ($\geq 1-fj$). This is done to optimize the sensitivity of the analysis as the signal to background ratio (S/B) is greater for the $\geq 1-fj$ region than the $0-fj$ region.

Both models consist of one input layer, three densely connected node layers (Dense layer) and one output layer. The input layers have nodes for each input feature. The NN for 0- fj events has 16 input features while the NN for ≥ 1 - fj events has 27 due to additional variables of the forward jets. The activation function for the Dense layers is the Leaky Rectified Linear Unit (ReLU) function $f(x)$:

$$f(x) = \begin{cases} x, & \text{for } x \geq 0 \\ 0.5x, & \text{for } x < 0. \end{cases}$$

For the output layer, the activation function is the sigmoid function $\sigma(x)$:

$$\sigma(x) = \frac{1}{1 + e^{-x}}.$$

Finally, the **Adam** algorithm is used as the optimizer for updating the weights in the NN [20]. Figure 5.1 displays the described architecture of the NN models.

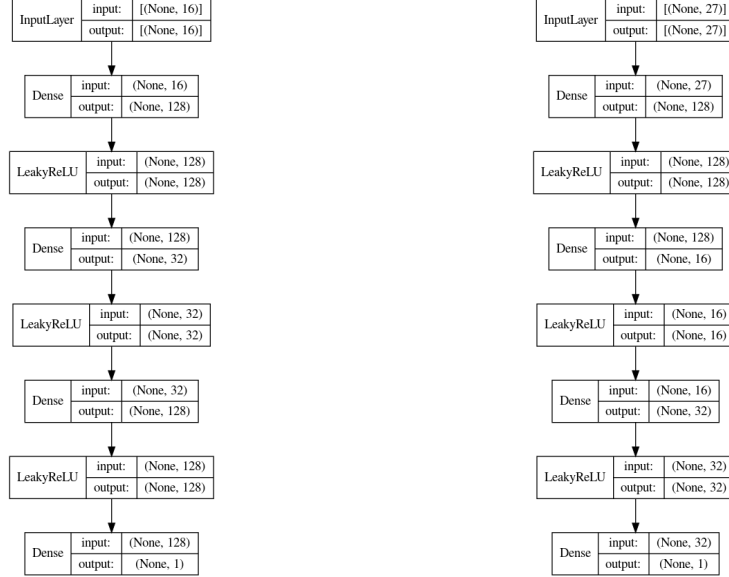


Figure 5.1: Visualization of the NN architecture for the zero forward jet region (left) and the ≥ 1 forward jets region (right).

5.3 Input features for the neural network

For the $tq\gamma$ process, it is not easy to find characteristic variables that distinguish this process from background processes. This is due to the small S/B ratio of the process

5.3 Input features for the neural network

and the similarity of some background processes. A different neural network based approach was used to find features that have the most discriminatory power.

The final input features used for the two NN models for discrimination are listed in Table 5.1 and 5.2 for the $0\ fj$ and $\geq 1\ fj$ regions respectively.

	0 fj variables	Explanation
0	HT	Scalar sum of all trasnverse momenta
1	blep_dr	ΔR of b -jet and lepton
2	bph_pt	Transverse momentum of photon+ b -quark
3	lbj_eta	$ \eta $ of leading b -jet
4	lbj_pt	p_T of leading b -jet
5	lbj_tagWeightBin _DL1r_Continuous	
6	lep1_eta	p_T of leading lepton
7	lep1_id	ID to determine lepton type
8	lep-ph_dr	ΔR distance between lepton and photon
9	met_met	Missing transverse energy
10	ph_eta	η of the photon
11	ph_pt	p_T of the photon
12	top_m	invariant mass of top quark
13	top-ph_pt	Summed p_T of top quark and photon
14	transMassWb	transverse mass of lepton, b -jet and neutrino
15	transMassWph	transverse mass of photon and W boson

Table 5.1: Input variables of the NN for events with no forward jets alongside their explanation.

	≥ 1 fj variables	Explanation
0	HT	See Table 5.1
1	Wbsn_e	Energy of W boson
2	bfj_m	Invariant mass of b -jet and forward jet
3	blep_dr	See Table 5.1
4	blep_m	Invariant mass of b -jet and lepton
5	bph_m	Invariant mass of b -jet and photon
6	fj_eta	$ \eta $ of forward jet
7	fj_phi	ϕ of forward jet
8	fjet_flag	forward jet is jet with highest p_T in event
9	fjph_ctheta	$\cos(\theta)$ between photon and forward jets
10	fjph_deta	Distance in $ \eta $ between forward jet and photon
11	fjph_dr	ΔR distance between forward jet and photon
12	fjph_e	Energy of forward jet and photon
13	fjph_m	Invariant mass of forward jet and photon
14	lbj_eta	See Table 5.1
15	lbj_phi	ϕ of leading b -jet
16	lbj_pt	See Table 5.1
17	lbj_tagWeightBin _DL1r_Continuous	See Table 5.1
18	lep1_eta	See Table 5.1
19	lep1_pt	p_T of leading lepton
20	met_met	See Table 5.1
21	met_phi	ϕ of missing transverse momentum
22	ph_phi	ϕ of photon
23	ph_pt	See Table 5.1
24	top_m	See Table 5.1
25	topph_ctheta	$\cos(\theta)$ between top quark and photon
26	transMassWb	See Table 5.1

Table 5.2: Input variables of the NN for events with at least one forward jet alongside their explanation.

5.4 Performance and distribution of the NN output

The distribution of the NN output for $\geq 1-fj$ is displayed in Figure 5.2. In this plot, the contributions from different signal and background MC samples are shown and stacked on top of each other. The data samples are viewed separately and also added to the plot. These plots confirm that the S/B ratio is larger in bins with higher NN output values.

To determine the performance of the NN output, background suppression is plotted against the signal efficiency at different cut values on the NN output in a receiver operating characteristic (ROC) curve in Figure 5.3. The signal efficiency (SE) is calculated as follows:

$$SE = \frac{\text{Number of true signal events}}{\text{Total number of signal events}}$$

and the background suppression (BS) is calculated with the formula

$$BS = 1 - \frac{\text{Number of true background events}}{\text{Total number of background events}}$$

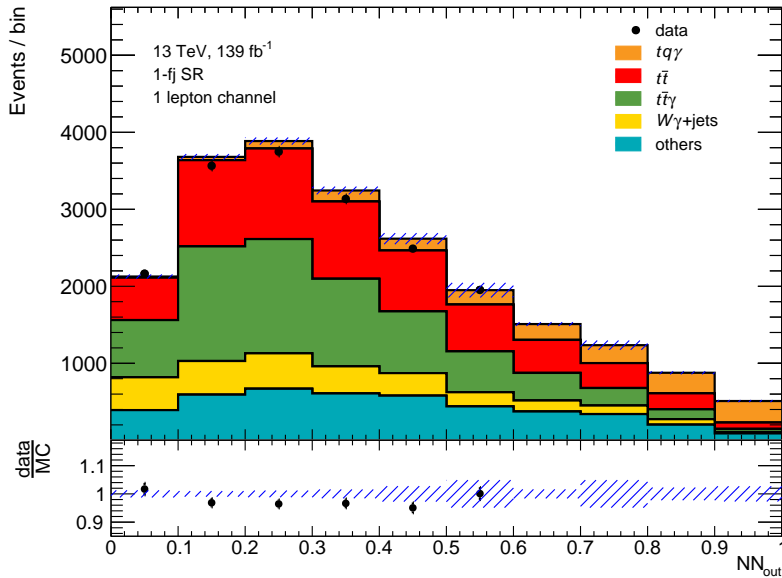


Figure 5.2: Visualisation of the NN output event distribution.

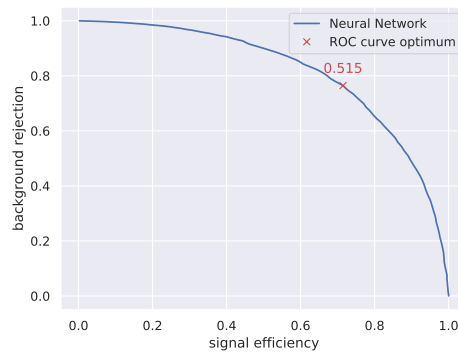


Figure 5.3: ROC curve of the neural network with the point of maximized signal efficiency and background rejection, which is the closest data point to the (1,1) corner.

6 Differential analysis of the NN output

6.1 Weighted correlations of input features with the NN output

6.1.1 Motivation for calculating correlations

Correlations between input variables and the neural network's provide an overview of what the NN has "learned". They represent which input variables have the strongest influence on the output of the NN. The level of influence of any input variable is determined during the training phase of the NN. For example, suppose the value of a specific input variable turns out to be an essential parameter in the discrimination of the signal from the background. In that case, this variable will acquire a strong correlation after the training process. Consequently, strongly correlated variables would provide a critical basis to determine which properties of the $tq\gamma$ process help in understanding the photon to top quark coupling.

6.1.2 Steps of calculation

Weighted correlations between two sets of data are calculated by first determining the covariance of these sets. For the covariance, the weighted mean of each set is needed. The weighted mean is calculated as follows

$$m(x; w) = \frac{\sum_i w_i x_i}{\sum_i w_i}$$

where x is the given set over which to calculate the mean. In this section, x represents one input feature of a process or the NN output values. The weights of each data point is given by w . The covariance is then calculated with the formula

$$cov(x, y; w) = \frac{\sum_i w_i \cdot (x_i - m(x; w)) \cdot (y_i - m(y; w))}{\sum_i w_i}.$$

Here, y stands for the second data set. Finally, the weighted correlation is then determined to be

$$\text{corr}(x, y; w) = \frac{\text{cov}(x, y; w)}{\sqrt{\text{cov}(x, x; w) \cdot \text{cov}(y, y; w)}}.$$

Thus, the correlation between the values for one input feature X_{input} and the NN output values Y_{output} with the weights W would be $\text{corr}(X_{\text{input}}, Y_{\text{output}}; W)$.

Calculations for the $0 \text{ } fj$ region and the $\geq 1 \text{ } fj$ region are done separately. Every generated event is saved with 110 different event features, including the input features, the NN output value and the NN weights. As most event features are not considered in this thesis, the explanation for features that are not part of the input is not provided.

At the start, the calculation for variable correlations with the NN output is performed for all events of the same process. Then, all correlations of the background samples are merged. This is done by calculating a weighted mean over all samples. Here, the sum of weights in a sample is used as the new weight for the mean. Finally, the correlation of measured data is also determined. The final result is a correlation table for the whole background, the $tq\gamma$ process and the measured data in each forward jet region. The result of the calculations is visualised and discussed in Section 6.1.3.

6.1.3 Results of the correlation calculations

The results of the calculations are listed in Table 8.1 of the Appendix. This table also contains some correlations of features that are not part of the input of the NN in the given region. Figure 6.1 and Figure 6.2 display correlations of the input features in order for both forward jet regions respectively. The correlations for all 110 event features are depicted in the Appendix in Figure 8.7.

The Figures show that forward jet (fj) features, specifically the $fj + \text{photon}$ energy ($fjph_e$) and the fj flag (fj_flag), have the strongest correlation. This confirms expectations as S/B is larger in the $\geq 1 \text{ } fj$ region. Furthermore, it is clear that some input features have no significant correlation at all. However, it is important to keep these features as part of the NN input as correlations among input variables significantly effect the NN output too. One more noteworthy aspect, is that the correlation of the forward jet energy parameter (fj_e in Figure 8.7 of the Appendix) has similar correlations to the $fj + \text{photon}$ energy ($fjph_e$) input feature. The fj_e parameter is slightly less correlated than $fjph_e$. This is due the additional small correlation of the photon energy in $fjph_e$. This aspect gives strong evidence for the correctness of the calculations.

6.1 Weighted correlations of input features with the NN output

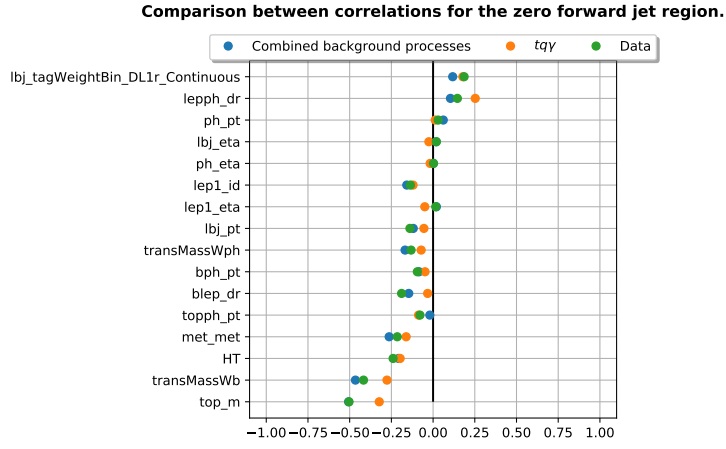


Figure 6.1: Visualisation of the correlations of input variables with the NN output in the $0\ fj$ region for the background samples, $tq\gamma$ and the measured data.

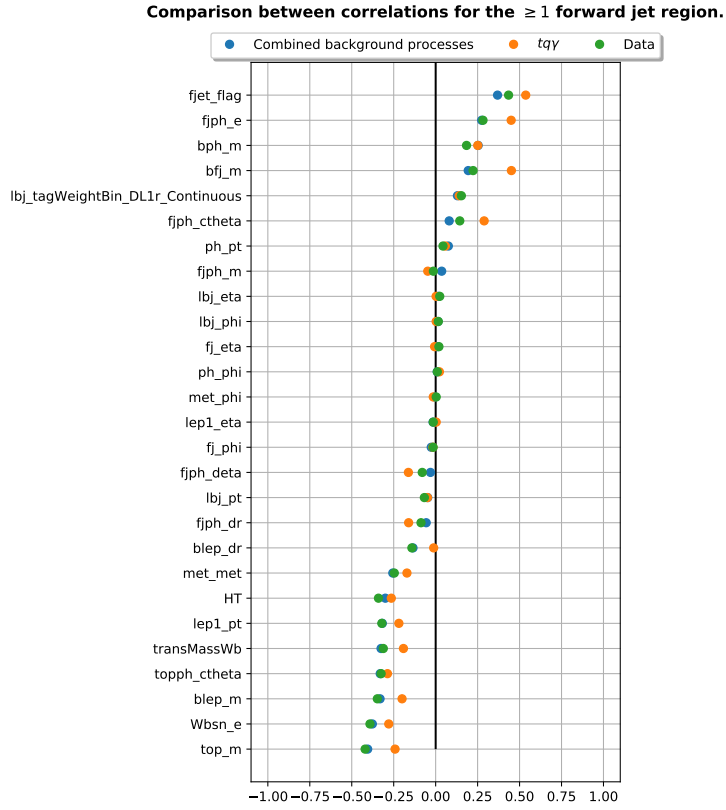


Figure 6.2: Visualisation of the correlations of input variables with the NN output in the $\geq 1\ fj$ region for the background samples, $tq\gamma$ and the measured data.

6.2 NN output distribution dependence on photon p_T^γ and fjet+photon energy $E_{fj+\gamma}$

To accommodate for the page limit of this thesis, most Figures in this section are provided in the Appendix.

In this section, two input variables are chosen to analyse the influence on the NN output further. In the first part of the analysis, an energy region for the input variables is chosen. Then, only events within that energy region are considered. This will be referred to as a "cut" throughout this section. After the cut, the distribution of the NN output is plotted to determine any noticeable changes. Additionally, a threshold for the NN output is chosen, and events above the threshold are examined. The $tq\gamma$ above the threshold must not exceed a statistical error $\frac{N_{\text{signal}}}{\sqrt{N_{\text{signal}}}}$ of over 10%. The composition of events above the threshold is then visualised and discussed. Finally, changes in signal and background compositions are examined. For simplicity and better sensitivity, only the ≥ 1 forward jet region is considered in this analysis.

To compare with the NN output before any cut is applied, the Figure 8.2 gives the composition of the NN output for two different thresholds. One at $NN = 0.9$ and the other at the highest possible threshold before the statistical error becomes too high. The same thresholds are used in other composition plots of this analysis.

The first input variable that is to be analysed is the photon's transverse momentum p_T^γ . As the $tq\gamma$ process is sensitive to the top quark to photon coupling, analysing the output dependence of the momentum of the photon provides an excellent way to test this prediction. The distribution of p_T^γ is shown in Figure 6.3.

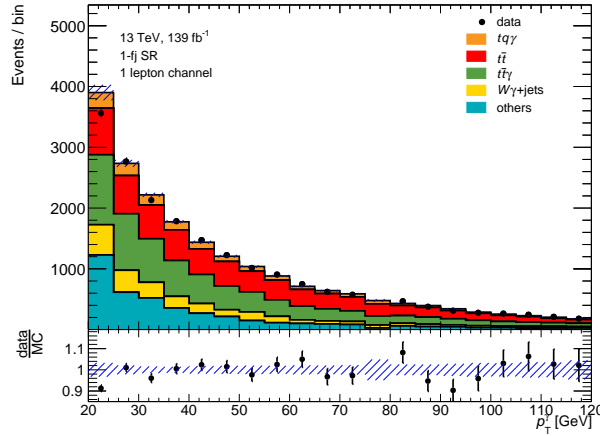


Figure 6.3: Distribution of the transverse momentum of the photon p_T^γ .

Results from subsection 6.1.3 give a low correlation of p_T^γ at around 5.8% for the $tq\gamma$ sample in the $\geq 1 fj$ region. The dependence of the NN output on p_T^γ is therefore found not to be significant. With the help of the distribution, it is chosen to cut p_T^γ at 40 GeV. The positive correlation predicts that higher values for p_T^γ result in a better signal-background discrimination in the NN output. The NN output distribution for events with $p_T^\gamma \geq 40$ GeV is displayed in Figure 8.3. The composition after two different thresholds is shown in Figure 8.4.

When comparing Figures 8.1 and 8.3 it is noticeable that S/B does increase for higher values of p_T^γ but the difference is not significant and is not examined further. More noticeable differences are seen when comparing Figures 8.2 and 8.4. Here, it can be clearly seen that the percentage of $t\bar{t}$ in the background is substantially higher (jumps from 35.8% to 47.8%). This suggests that the $t\bar{t}$ has a p_T^γ for the falsely reconstructed photon of this process. Without a deeper analysis, no more statements can be made on this incident. In addition, the contributions of less significant background processes, which are depicted in the category "other", do get suppressed. The 38.8% background contribution of this category falls to 26% for the p_T^γ cut.

The second input variable is the sum of the photon and forward jet energies $E_{fj+\gamma}$. This input feature has the second most strongest correlation with the NN output for the signal sample at around 44.99%. Because of its high correlation, $E_{fj+\gamma}$ is an important candidate variable that may be essential in the understanding of the top+photon coupling. It is also important to analyse a strongly correlated variable alongside a weakly correlated variable to test nature of the NN output and variables at different limits.

The distribution of $E_{fj+\gamma}$ is shown in Figure 6.4. $E_{fj+\gamma}$ is chosen to be cut to the region $E_{fj+\gamma} \geq 900$ GeV. The high positive correlation of $E_{fj+\gamma}$ predicts a greater discrimination between signal and background for larger energy values the variable. This is verified by the NN output distribution after the cut in Figure 8.5. It is clear that the S/B ratio is significantly higher for $NN > 0.5$. These results confirm that strongly correlated variables have stronger influences on the signal-background discrimination of the NN. The composition of the events above the two different thresholds is depicted in Figure 8.6. Here, there is no significant change seen in the composition of the main background as it was the case with the cut on p_T^γ .

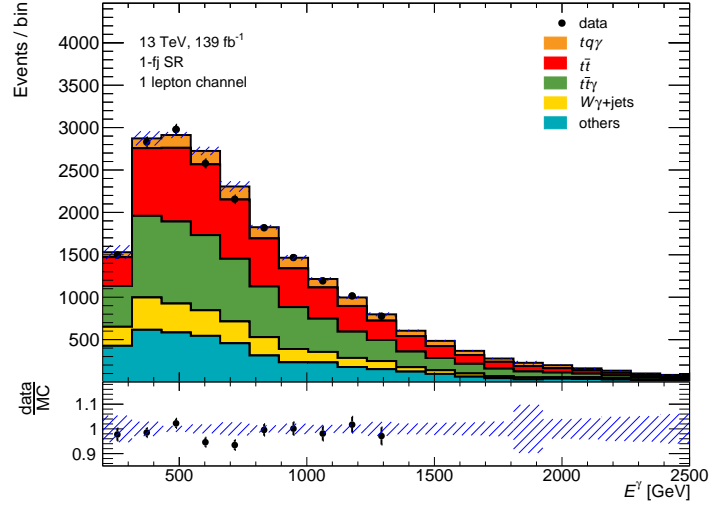


Figure 6.4: Distribution of the forward jet + photon energy $E_{fj+\gamma}$.

7 Conclusion

The study in this thesis has been conducted regarding a differential measurement of the single top quark production in association with a photon of the Standard Model to closer examine the electromagnetic coupling of the top quark. Analyses of the electromagnetic coupling of the top quark provide important tests to the Standard Model. This analysis aimed to use a neural network, used for signal-background discrimination, to find variables sensitive to the top quark's EM coupling.

The influence of different input variables on the NN has been thoroughly analyzed. It has been calculated how the characteristic features of the $tq\gamma$ process correlate with the output. Highly correlated and less correlated features are identified, and the reasons for high or low correlation are discussed. Most correlations follow the expectations, verifying the correctness of the calculations.

Two input features, the transverse momentum of the photon p_T^γ and the sum of the forward jet energies and the photon energy $E_{fj+\gamma}$, have been further examined. These features are examples of a strongly correlated and a weakly correlated variable to test the nature of the NN at borderline cases. This is useful to determine whether the NN needs adjustment. For p_T^γ , it has been found that higher divisions in energy, such as the division into the region $p_T^\gamma > 40$ GeV, result in a greater S/B ratio in the NN output than lower energy divisions. While this observation is significant, it is not as substantial as the effects of divisions for the $E_{fj+\gamma}$ input feature. The much higher correlation of $E_{fj+\gamma}$ leads to more significant changes in the NN output for different divisions. For this feature, it is again found that higher energies, such as the region $E_{fj+\gamma} > 900$ GeV, ensues a significantly larger S/B in the NN output.

This thesis provides an essential framework for the differential measurement of $tq\gamma$ with the full Run-2 dataset of the LHC. It suggests characteristic features that could be sensitive to the EM coupling of the top quark. In addition, it also confirms that the significance of divisions on input features coincide with the calculated correlations. The framework provided by this thesis may be used to inspect the input variables further. Regarding future studies, conducting the so-called *distance correlation* [19] may provide further indications to whether the NN needs to be adjusted.

8 Appendix

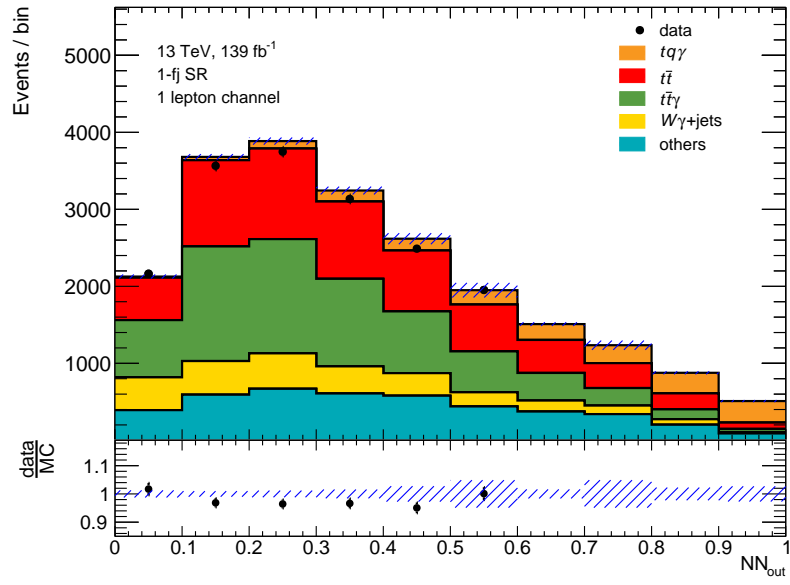


Figure 8.1: Visualisation of the NN output's event distribution.

Event parameter	0 fj region			≥ 1 fj region		
	Background	$tq\gamma$	Data	Background	$tq\gamma$	Data
top_m	-0.51	0.01	0.03	-0.41	0.06	0.04
Wbsn_e	-0.35	-0.02	0.00	-0.38	0.00	-0.00
blep_m	-0.39	0.01	0.01	-0.33	0.02	0.01
topph_ctheta	-0.28	-0.00		-0.33	-0.01	0.02
transMassWb	-0.47	-0.00		-0.33	-0.02	-0.02
lep1_pt	-0.36			-0.32	0.54	0.43
HT	-0.21	-0.24	-0.35	-0.30	-0.22	-0.32
met_met	-0.26	-0.05	0.02	-0.26	0.00	-0.01
topph_pt	-0.02	-0.12	-0.14	-0.18	-0.06	-0.03
blep_dr	-0.15	-0.06	-0.14	-0.14	-0.05	-0.07
bph_pt	-0.08	-0.03	0.02	-0.13	0.00	0.02
transMassWph	-0.17	0.00	-0.00	-0.10	0.00	0.02
fjph_dr	0.00	0.18	0.19	-0.06	0.14	0.15
lbj_pt	-0.12	-0.32	-0.50	-0.05	-0.24	-0.42
fjph_deta	0.00	-0.36	-0.29	-0.03	-0.29	-0.33
fj_phi	-0.00	-0.09	-0.08	-0.03	-0.11	-0.19
lep1_eta	0.02	-0.30	-0.37	-0.02	-0.28	-0.39
met_phi	0.00	0.27	0.14	-0.01	0.25	0.18
lep1_id	-0.16	-0.27	-0.43	-0.00	-0.20	-0.35
ph_eta	0.00			0.00	0.45	0.22
ph_phi	-0.00	-0.05	-0.09	0.01	-0.08	-0.13
fj_eta	-0.00			0.01	-0.05	-0.01
lbj_phi	-0.00	0.07	0.03	0.01	0.45	0.28
lbj_eta	0.02	-0.02	0.00	0.02	-0.16	-0.09
fjph_m		-0.02	0.00	0.04	-0.16	-0.08
ph_pt	0.06			0.08	0.29	0.14
fjph_ctheta		0.25	0.15	0.08	0.12	0.12
lepph_dr	0.10	-0.03	-0.19	0.11	-0.01	-0.14
lbj_tagWeightBin _DL1r_Continuous	0.12	-0.16	-0.21	0.13	-0.17	-0.25
bfj_m		0.02	-0.00	0.19	-0.01	0.00
bph_m	0.19	-0.20	-0.24	0.25	-0.26	-0.34
fjph_e	0.04	-0.07	-0.13	0.27	-0.03	-0.10
fjet_flag		-0.28	-0.42	0.37	-0.19	-0.31

Table 8.1: List of correlations between samples and the NN output in the zero forward jet region as well as samples in the ≥ 1 forward jet region.

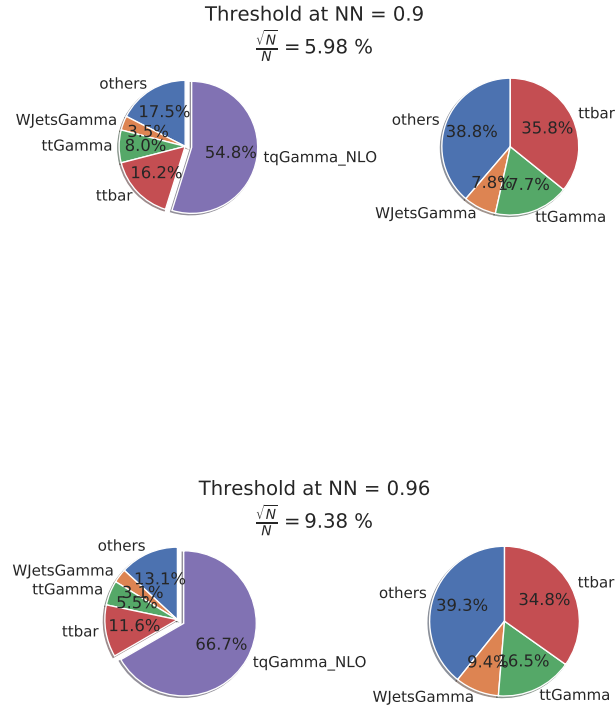


Figure 8.2: Composition of NN output for two different thresholds without any cuts applied. The right pie chart gives the composition without of the background.

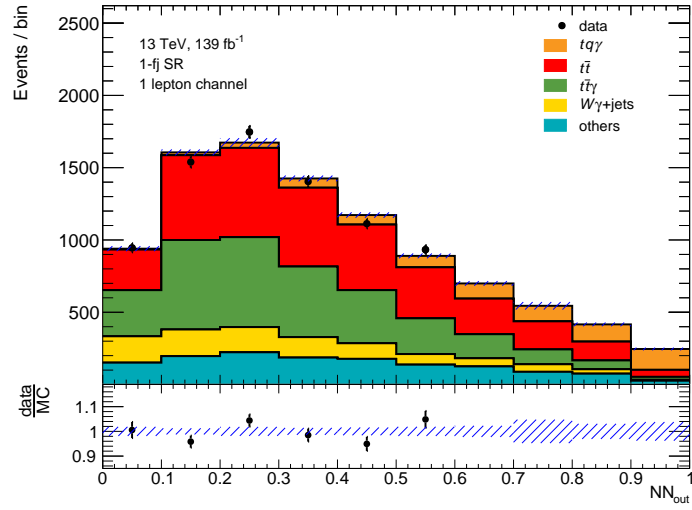


Figure 8.3: NN output distribution for the $p_T^\gamma \geq 40$ GeV region.

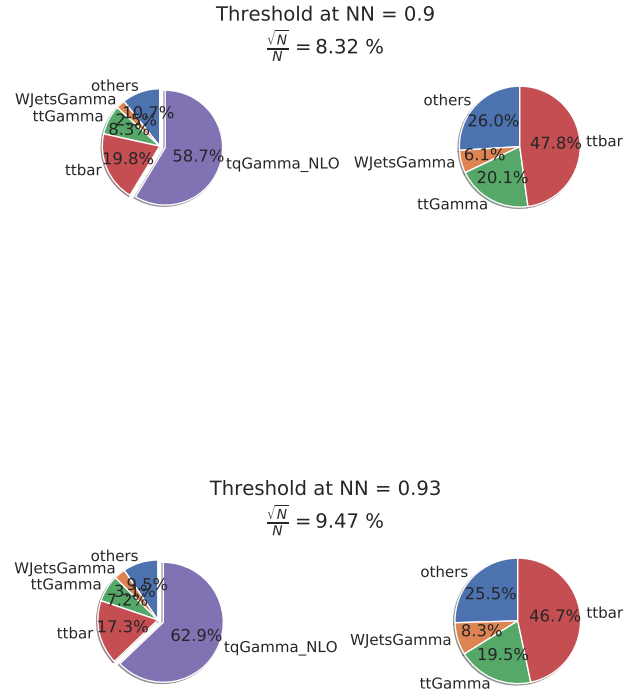


Figure 8.4: Composition of NN output for two different thresholds in the region $p_T^\gamma \geq 40$ GeV.

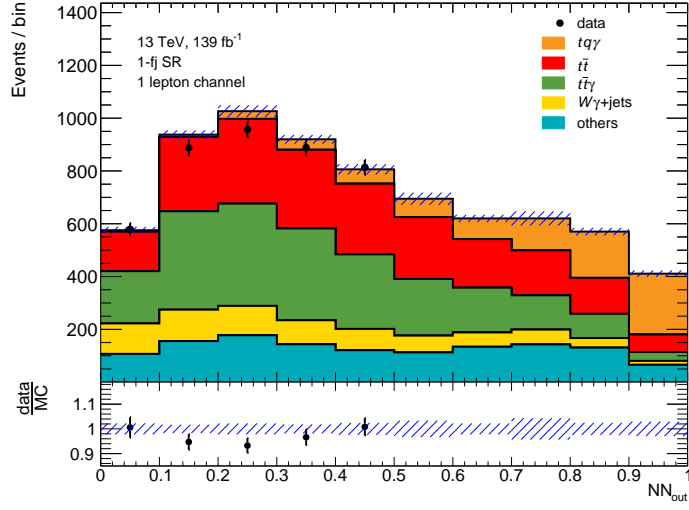


Figure 8.5: NN output distribution for the $E_{fj+\gamma} \geq 900$ GeV region.

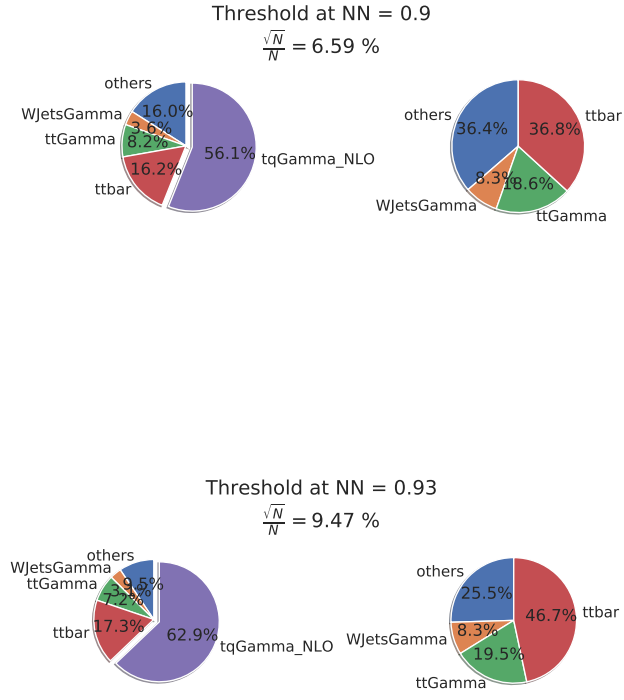


Figure 8.6: Composition of NN output for two different thresholds in the region $E_{fj+\gamma} \geq 900$ GeV.

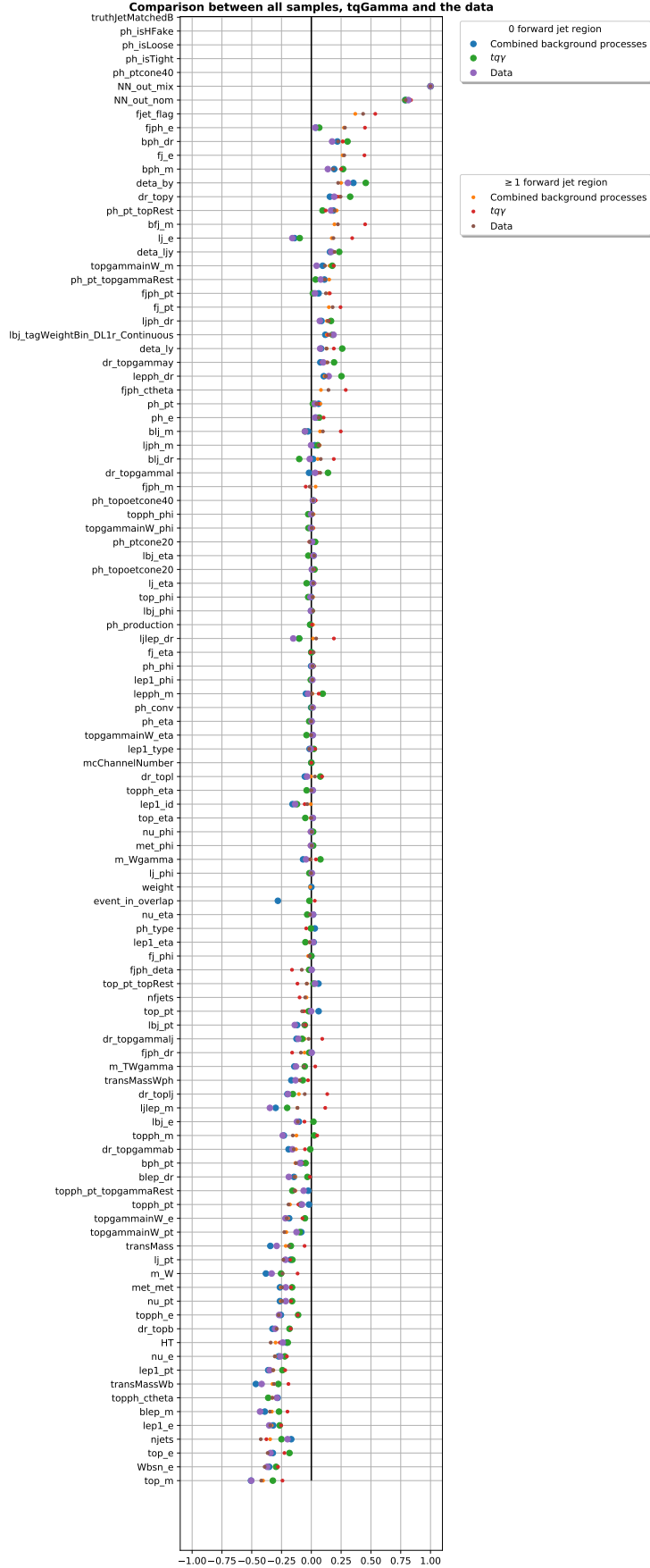


Figure 8.7: Correlations of all event properties with the NN output in the 0 fj and ≥ 1 fj region for the background samples, $tq\gamma$ and the measured data.

9 Danksagung

Zu aller erst möchte ich mich bei Herrn Priv.-Doz. Dr. Johannes Erdmann bedanken, der mir überhaupt ermöglicht hat, diese Bachelorarbeit in dem Lehrstuhl für Experimentelle Physik IV zu schreiben, mich Monate vorher über potentielle Aufgaben und dem Ablauf der Arbeit unterrichtet und mein Interesse an das Thema stets aufrecht erhalten hat.

Ich möchte mich auch bei Björn Wendland und Nils Julius Abicht bedanken, die meinen Fortschritt im Auge behalten haben, um den Abschluss der Arbeit zu garantieren, und meine Zwischenergebnisse korrekturgelesen haben.

Des Weiteren möchte ich mich bei Herrn Prof. Dr. Johannes Albrecht für die Zweitgutachtung herzlich bedanken.

Abschließend, bedanke ich mich bei meinen Freunden, die mir stetig in stressigen Momenten Unterstützung gegeben haben, ohne die diese Bachelorarbeit nicht gelungen wäre.

Bibliography

- [1] M. Aaboud et al. “Electron efficiency measurements with the ATLAS detector using 2012 LHC proton–proton collision data.” In: *The European Physical Journal C* 77.3 (Mar. 2017). ISSN: 1434-6052. DOI: 10.1140/epjc/s10052-017-4756-2. URL: <http://dx.doi.org/10.1140/epjc/s10052-017-4756-2>.
- [2] G. Aad et al. “Muon reconstruction performance of the ATLAS detector in proton–proton collision data at $\sqrt{s} = 13$ TeV.” In: *The European Physical Journal C* 76.5 (May 2016). ISSN: 1434-6052. DOI: 10.1140/epjc/s10052-016-4120-y. URL: <http://dx.doi.org/10.1140/epjc/s10052-016-4120-y>.
- [3] G. Aad et al. “Topological cell clustering in the ATLAS calorimeters and its performance in LHC Run 1.” In: *The European Physical Journal C* 77.7 (July 2017). ISSN: 1434-6052. DOI: 10.1140/epjc/s10052-017-5004-5. URL: <http://dx.doi.org/10.1140/epjc/s10052-017-5004-5>.
- [4] T. Aaltonen et al. “Observation of Electroweak Single Top-Quark Production.” In: *Phys. Rev. Lett.* 103 (9 Aug. 2009), p. 092002. DOI: 10.1103/PhysRevLett.103.092002. URL: <https://link.aps.org/doi/10.1103/PhysRevLett.103.092002>.
- [5] V. M. Abazov et al. “Observation of Single Top-Quark Production.” In: *Phys. Rev. Lett.* 103 (9 Aug. 2009), p. 092001. DOI: 10.1103/PhysRevLett.103.092001. URL: <https://link.aps.org/doi/10.1103/PhysRevLett.103.092001>.
- [6] S. Agostinelli et al. “Geant4—a simulation toolkit.” In: *Nuclear Instruments and Methods in Physics Research Section A: Accelerators, Spectrometers, Detectors and Associated Equipment* 506.3 (2003), pp. 250–303. ISSN: 0168-9002. DOI: [https://doi.org/10.1016/S0168-9002\(03\)01368-8](https://doi.org/10.1016/S0168-9002(03)01368-8). URL: <https://www.sciencedirect.com/science/article/pii/S0168900203013688>.
- [7] *ATLAS inner detector: Technical Design Report, 1*. Technical design report. ATLAS. Geneva: CERN, 1997. URL: <https://cds.cern.ch/record/331063>.
- [8] Amos Breskin and Rüdiger Voss. *The CERN Large Hadron Collider: Accelerator and Experiments*. Geneva: CERN, 2009. URL: <https://cds.cern.ch/record/1244506>.

- [9] Carsten Burgard. *Example: Standard model of physics*. Dec. 2016. URL: <https://texample.net/tikz/examples/model-physics/> (visited on 06/30/2021).
- [10] Matteo Cacciari, Gavin P Salam, and Gregory Soyez. “The anti-ktjet clustering algorithm.” In: *Journal of High Energy Physics* 2008.04 (Apr. 2008), pp. 063–063. ISSN: 1029-8479. DOI: 10.1088/1126-6708/2008/04/063. URL: <http://dx.doi.org/10.1088/1126-6708/2008/04/063>.
- [11] S. Chatrchyan et al. “The CMS Experiment at the CERN LHC.” In: *JINST* 3 (2008), S08004. DOI: 10.1088/1748-0221/3/08/S08004.
- [12] Francois Chollet et al. *Keras*. 2015. URL: <https://github.com/fchollet/keras>.
- [13] Thorsten Chwalek. “Messung der W-Boson-Helizitätsanteile in Top-Quark-Zerfällen mit dem CDF II Experiment und Studien zu einer frühen Messung des ttbar-Wirkungsquerschnitts mit dem CMS Experiment.” Presented 12 Feb 2010. 2010. URL: <https://cds.cern.ch/record/1416031>.
- [14] ATLAS Collaboration and Irinel Caprini. “Monitoring and data quality assessment of the ATLAS liquid argon calorimeter.” In: *JINST* 9 (May 2014). DOI: 10.1088/1748-0221/9/07/P07024.
- [15] The ATLAS Collaboration et al. “The ATLAS Experiment at the CERN Large Hadron Collider.” In: *Journal of Instrumentation* 3.08 (Aug. 2008), S08003–S08003. DOI: 10.1088/1748-0221/3/08/s08003. URL: <https://doi.org/10.1088/1748-0221/3/08/s08003>.
- [16] Tevatron Electroweak Working Group. *Combination of CDF and D0 Measurements of the Single Top Production Cross Section*. 2009. arXiv: 0908.2171 [hep-ex].
- [17] *Identification of Jets Containing b-Hadrons with Recurrent Neural Networks at the ATLAS Experiment*. Tech. rep. All figures including auxiliary figures are available at <https://atlas.web.cern.ch/Atlas/GROUPS/PHYSICS/PUBNOTES/ATL-PHYS-PUB-2017-003>. Geneva: CERN, Mar. 2017. URL: <https://cds.cern.ch/record/2255226>.
- [18] *Identification of Jets Containing b-Hadrons with Recurrent Neural Networks at the ATLAS Experiment*. Tech. rep. All figures including auxiliary figures are available at <https://atlas.web.cern.ch/Atlas/GROUPS/PHYSICS/PUBNOTES/ATL-PHYS-PUB-2017-003>. Geneva: CERN, Mar. 2017. URL: <https://cds.cern.ch/record/2255226>.
- [19] Gregor Kasieczka and David Shih. “Robust Jet Classifiers through Distance Correlation.” In: *Phys. Rev. Lett.* 125 (12 Sept. 2020), pp. 35–38. DOI: 10.1103/PhysRevLett.125.122001. URL: <https://link.aps.org/doi/10.1103/PhysRevLett.125.122001>.

-
- [20] Diederik P. Kingma and Jimmy Ba. *Adam: A Method for Stochastic Optimization*. 2017. arXiv: 1412.6980 [cs.LG].
 - [21] W Lampl et al. *Calorimeter Clustering Algorithms: Description and Performance*. Tech. rep. All figures including auxiliary figures are available at <https://atlas.web.cern.ch/Atlas/GROUPS/PHYSICS/PUBNOTES/ATL-LARG-PUB-2008-002>. Geneva: CERN, Apr. 2008. URL: <https://cds.cern.ch/record/1099735>.
 - [22] Martín Abadi et al. *TensorFlow: Large-Scale Machine Learning on Heterogeneous Systems*. Software available from [tensorflow.org](https://www.tensorflow.org). 2015. URL: <https://www.tensorflow.org/>.
 - [23] A. M. Sirunyan et al. “Evidence for the Associated Production of a Single Top Quark and a Photon in Proton-Proton Collisions at $\sqrt{s} = 13$ TeV.” In: *Phys. Rev. Lett.* 121 (22 Nov. 2018), p. 221802. DOI: 10.1103/PhysRevLett.121.221802. URL: <https://link.aps.org/doi/10.1103/PhysRevLett.121.221802>.
 - [24] A. M. Sirunyan et al. “Evidence for the Associated Production of a Single Top Quark and a Photon in Proton-Proton Collisions at $s=13$ TeV.” In: *Physical Review Letters* 121.22 (Nov. 2018). ISSN: 1079-7114. DOI: 10.1103/physrevlett.121.221802. URL: <http://dx.doi.org/10.1103/PhysRevLett.121.221802>.
 - [25] P.A. Zyla et al. “Review of Particle Physics.” In: *PTEP* 2020.8 (2020), p. 083C01. DOI: 10.1093/ptep/ptaa104.

